Quantum Electronics **51** (8) 730–743 (2021)

https://doi.org/10.1070/QEL17522

A theoretical study of the group refractive index n_g in a four-level inverted Y-type system formed by ^{87}Rb atom–laser radiation interaction

R. Hazra, M.M. Hossain

Abstract. **We report a theoretical investigation of the dispersion resulting from electromagnetically induced transparency (EIT) and the associated group refractive index profiles n_g of a four-level inverted Y-type system formed by the interaction of three optical fields (probe, pump and control) with ^{87}Rb atoms. The density matrix equations are derived from the semi-classical Liouville's equation and solved both numerically and analytically to study the coherent nonlinear optical properties of the medium. We first present the EIT, dispersion and corresponding group index profiles n_g under the switch-on/off and on/off-resonance conditions of the pump and control lasers. In presence of both pump and control lasers, an enhancement of the EIT window, a sharp EIT spike and related steeper dispersion slopes are obtained at the line centre of the probe frequency detuning. The group index profiles with the variation of the strengths of individual applied optical fields are studied. The effect of the ground state decoherence rates on the group index profile is examined in detail. It is found that the manipulation of n_g values and the corresponding group velocities v_g of the probe light can be easily controlled from subluminal to superluminal values or vice versa by changing the strengths of the applied fields and the ground state decoherence rates. Besides, the EIT-based 'optical switching' phenomenon in the medium is explained by studying the variation of the group index with the pump and control Rabi frequencies.**

Keywords: *electromagnetically induced transparency, dispersion, group refractive index n_g, density matrix, Rb atoms, slow and fast light.*

1. Introduction

The group refractive index or group index n_g of an atomic medium is associated with the dispersive properties of the medium. In recent years, the study of group index and the related group velocity v_g have gained considerable attention of researchers due to a possibility of manipulating slow (subluminal) and fast (superluminal) light propagation through an atomic medium [1]. Theoretically, the dispersion of an atomic medium is calculated from the real part of the complex susceptibility of the medium. The positive or negative slope of the dispersion curve provides an increasing or decreasing value of the group index, respectively, which can be achieved by observing the coherence phenomena, such as electromagnetically induced transparency (EIT) [1–5], coherent population trapping (CPT) [6, 7], electromagnetically induced absorption (EIA) [8, 9], spontaneously generated coherence (SGC) [10, 11], etc. Particularly, the EIT phenomenon has received great attention due to its significantly narrow spectral linewidth and enhanced nonlinearity. Consequently, the slope of the EIT related dispersion signal becomes steeper with a higher amplitude. As a result, the dispersion and the related group index or group velocity are studied by observing the EIT phenomenon in alkali atoms like Rb, Cs, etc.

The studies on EIT are carried out in different atom–laser coupling schemes, for example, starting from basic three-level systems (Λ, V and Ξ) to four-, five- and higher-level systems [12–15]. Some studies of EIT and its dispersion were also performed in a combined system of some three- or four-level sub-systems [16–18]. The four-level inverted Y-type system is one such combined system that is formed by an amalgamation of a three-level lambda (Λ) and three-level cascade (Ξ) type sub-systems [19–24]. Various coherence phenomena have been studied in inverted Y-type systems [19–26] since its theoretical proposal by Joshi et al. [19]. In Ref. [19], the authors have studied the EIT and related dispersive properties and demonstrated the controllability of EIT and its dispersion under various parametric conditions. Liu et al. [20] have theoretically investigated the generation of optical solitons in an inverted Y-type system by manipulating the ultraslow group velocities of light. The manipulation of dispersive properties was also used for the demonstration of phase gates and for achieving optical Kerr-nonlinearity in an inverted Y-type configuration [21]. Some other studies using the dispersive properties of an inverted Y-type system have been performed based on the control of optical bistability and optical switching [22]. Recently, Yadav et al. [23] have shown that the subluminal and superluminal light propagation in an inverted Y-type system of ^{87}Rb atoms is governed by the positive and negative values of the group refractive index and concluded that the control of the dispersive properties is more flexible in this type of system owing to the presence of the coupling fields. In Ref. [24], an experimental investigation was also carried out in a four-level inverted Y-type system using hyperfine levels of ^{87}Rb atoms and the experimental results provided signatures of manipulating absorption and disper-

R. Hazra, M.M. Hossain Department of Physics, Aliah University, II A/27, New Town, Kolkata-700160, India;
e-mail: mhossain.phy@gmail.com, mhossain.phys@aliah.ac.in

Received 25 January 2021; revision received 7 July 2021
Kvantovaya Elektronika **51** (8) 730–743 (2021)
Submitted in English

sion windows in the medium by the control of the coupling fields. Moreover, single EIT, double EIT and related dispersion profiles, group index, group velocity, subluminal and superluminal propagation of light have also been studied in an inverted Y-type system [25, 26].

In this paper, our main objective is to study various effects on the group index profiles of a four-level inverted Y-type configuration in ^{87}Rb atomic medium which are less explored in the earlier works. The four-level inverted Y-type system is formed by the coupling of a weak probe, a strong pump and a strong control laser fields in the hyperfine levels of the $5S_{1/2} \leftrightarrow 5P_{1/2} \leftrightarrow 5D_{3/2}$ transitions of ^{87}Rb atoms. It is to be noted that the proposed inverted Y-type system is a combination of two sub-systems, namely, a three-level lambda (Λ) and a three-level cascade (Ξ) type sub-systems. Theoretically, the density matrix equations are derived from the semi-classical Liouville's equation of motion and solved numerically as well as analytically under steady-state conditions. First, we study the EIT and its dispersion spectra and the associated group index under switch-on/off and on/off-resonance conditions of the pump and control laser fields. Next, we study the effects of the individual strengths of the pump, control and probe fields on the group index profiles as a function of the probe detuning under the on-resonance condition of the pump and control lasers. The variation of group index profiles with the ground state decoherence rates is also studied in detail. Few numerically obtained results are compared with the analytically obtained ones. Finally, the phenomenon of EIT-based 'optical switching' is explained by studying the behaviour of the group index and probe absorption profiles as a function of the strength of the pump and control fields under off-resonance conditions.

2. Theoretical model

Figure 1 shows a four-level inverted Y-type system that is formed by the interaction of ^{87}Rb atoms with three laser fields, namely probe, pump and control lasers. Here, a weak probe laser field (frequency ω_{pr}) couples the ground state $|1\rangle$ ($5S_{1/2}$, $F = 1$) with the excited state $|3\rangle$ ($5P_{1/2}$, $F' = 2$), a strong pump laser field (frequency ω_p) couples the ground state $|2\rangle$ ($5S_{1/2}$, $F = 2$) with the common excited state $|3\rangle$ and a strong control laser field (frequency ω_c) couples the common excited state $|3\rangle$ with a higher excited state $|4\rangle$ ($5D_{3/2}$, $F'' = 3$). It is found that the pump and probe lasers form a three-level Λ-type sub-system with the levels $|1\rangle$, $|2\rangle$ and $|3\rangle$, whereas the control and probe lasers form a three-level Ξ-type sub-system with the levels $|1\rangle$, $|3\rangle$ and $|4\rangle$. The frequency detunings of the probe, pump and control laser fields are defined by $\Delta_{pr} = \omega_{pr} - \omega_{31}$, $\Delta_p = \omega_p - \omega_{32}$ and $\Delta_c = \omega_c - \omega_{43}$, respectively. We define the Rabi frequencies corresponding to the probe, pump and control fields as, $\Omega_{pr} = \boldsymbol{\mu}_{13} \cdot \boldsymbol{E}_{pr}/\hbar$, $\Omega_p = \boldsymbol{\mu}_{23} \cdot \boldsymbol{E}_p/\hbar$ and $\Omega_c = \boldsymbol{\mu}_{34} \cdot \boldsymbol{E}_c/\hbar$, respectively, where $\boldsymbol{\mu}_{ij}$ ($i \neq j$) are the dipole matrix elements and $\boldsymbol{E}_{pr}$, $\boldsymbol{E}_p$ and $\boldsymbol{E}_c$ are the electric field vectors associated with the probe, pump and control lasers coupling the dipole allowed levels $|1\rangle \rightarrow |3\rangle$, $|2\rangle \rightarrow |3\rangle$ and $|3\rangle \rightarrow |4\rangle$, respectively. The proposed four-level inverted Y-type scheme has already been experimentally realised in ^{87}Rb atoms [24], where the authors have studied the probe absorption and dispersion profiles for different strengths and detunings of the control lasers. However, our main objective is to study various effects on the dispersion-related group index profiles n_g which have not been previously studied. Here, it is to be mentioned that the polarisations and wavelengths of the incident beams may by considered the same as those from Ref [24] for experimentation. In Fig. 1, Γ_{31}, Γ_{32} and Γ_{43} are the radiative decay rates between the electric dipole allowed transitions $|3\rangle \rightarrow |1\rangle$, $|3\rangle \rightarrow |2\rangle$ and $|4\rangle \rightarrow |3\rangle$, respectively, whereas the terms Γ_{21} and Γ_{12} denote the nonradiative ground state decay rates between the electric non-dipole allowed ground levels $|2\rangle \rightarrow |1\rangle$ and $|1\rangle \rightarrow |2\rangle$, respectively. We consider the nonradiative decay rates among the ground states due to various natural phenomena, such as temperature fluctuation, atom-atom/wall collisions, buffer gas-induced collisions, collisional dephasing, etc., giving rise to 'decoherence' in the medium [27–29].

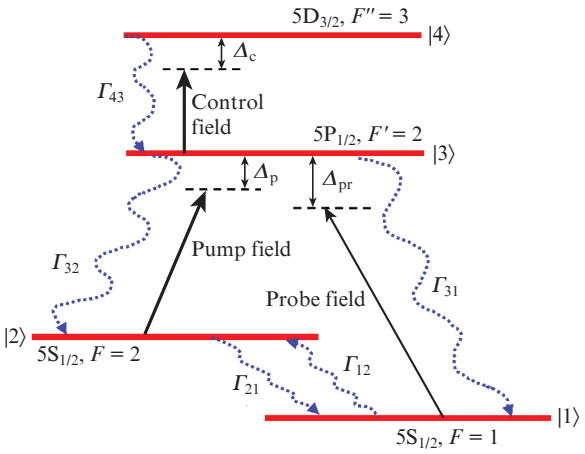

Figure 1. Schematic of a four-level inverted Y-type system formed in the hyperfine levels of $5S_{1/2} \leftrightarrow 5P_{1/2} \leftrightarrow 5D_{3/2}$ transitions of ^{87}Rb atoms by the coupling of a probe laser field with Rabi frequency Ω_{pr} from the ground state $|1\rangle$ ($5S_{1/2}$, $F = 1$) to an excited state $|3\rangle$ ($5P_{1/2}$, $F' = 2$), a pump laser with Rabi frequency Ω_p from the ground state $|2\rangle$ ($5S_{1/2}$, $F = 2$) to the common excited state $|3\rangle$ ($5P_{1/2}$, $F' = 2$) and a control laser with Rabi frequency Ω_c from the common excited state $|3\rangle$ ($5P_{1/2}$, $F' = 2$) to another higher excited state $|4\rangle$ ($5D_{3/2}$, $F'' = 3$).

To derive the density matrix equations, we use the well-known semi-classical Liouville's equation (see, for example, Refs [15, 30])

$$\frac{\partial \rho}{\partial t} = \frac{-i}{\hbar}[H, \rho] + \xi_{relax}\rho, \tag{1}$$

where ρ is the density matrix operator, and ξ_{relax} is the relaxation matrix operator in which all the radiative and nonradiative decay rates are included phenomenologically. The density matrix equations obtained from Eqn (1) under rotating wave approximation (RWA) have the form [15, 30]

$$\dot{\rho}_{11} = \frac{i\Omega_{pr}(\rho_{31} - \rho_{13})}{2} + \Gamma_{21}\rho_{22} + \Gamma_{31}\rho_{33} - \Gamma_{12}\rho_{11},$$

$$\dot{\rho}_{22} = \frac{i\Omega_p(\rho_{32} - \rho_{23})}{2} + \Gamma_{12}\rho_{11} + \Gamma_{32}\rho_{33} - \Gamma_{21}\rho_{22},$$

$$\dot{\rho}_{33} = \frac{i\Omega_{pr}(\rho_{13} - \rho_{31})}{2} + \frac{i\Omega_p(\rho_{23} - \rho_{32})}{2} - \frac{i\Omega_c(\rho_{34} - \rho_{43})}{2} -$$

$$-(\Gamma_{31}+\Gamma_{32})\rho_{33}+\Gamma_{43}\rho_{44},$$

$$\dot{\rho}_{44}=\frac{i\Omega_c(\rho_{34}-\rho_{43})}{2}-\Gamma_{43}\rho_{44}, \tag{2}$$

$$\dot{\rho}_{31}=[i\Delta_{pr}-\gamma_{31}]\rho_{31}+\frac{i\Omega_p}{2}\rho_{21}+\frac{i\Omega_c}{2}\rho_{41}+\frac{i\Omega_{pr}(\rho_{11}-\rho_{33})}{2},$$

$$\dot{\rho}_{21}=[i(\Delta_{pr}-\Delta_p)-\gamma_{21}]\rho_{21}+\frac{i\Omega_p}{2}\rho_{31}-\frac{i\Omega_{pr}}{2}\rho_{23},$$

$$\dot{\rho}_{32}=[i\Delta_p-\gamma_{32}]\rho_{32}+\frac{i\Omega_{pr}}{2}\rho_{12}+\frac{i\Omega_c}{2}\rho_{42}+\frac{i\Omega_p(\rho_{22}-\rho_{33})}{2},$$

$$\dot{\rho}_{41}=[i(\Delta_{pr}+\Delta_c)-\gamma_{41}]\rho_{41}+\frac{i\Omega_c}{2}\rho_{31}-\frac{i\Omega_{pr}}{2}\rho_{43},$$

$$\dot{\rho}_{42}=[i(\Delta_p+\Delta_c)-\gamma_{42}]\rho_{42}+\frac{i\Omega_c}{2}\rho_{32}-\frac{i\Omega_p}{2}\rho_{43},$$

$$\dot{\rho}_{43}=[i\Delta_c-\gamma_{43}]\rho_{43}-\frac{i\Omega_{pr}}{2}\rho_{41}-\frac{i\Omega_p}{2}\rho_{42}-\frac{i\Omega_c(\rho_{44}-\rho_{33})}{2}.$$

In Eqn (2), we redefine the decay rates as follows

$$\gamma_{31}=\frac{\Gamma_{31}+\Gamma_{32}+\Gamma_{12}}{2},$$

$$\gamma_{21}=\frac{\Gamma_{21}+\Gamma_{12}}{2},$$

$$\gamma_{32}=\frac{\Gamma_{31}+\Gamma_{32}+\Gamma_{21}}{2},$$

$$\gamma_{41}=\frac{\Gamma_{43}+\Gamma_{12}}{2},$$

$$\gamma_{42}=\frac{\Gamma_{21}+\Gamma_{43}}{2},$$

$$\gamma_{43}=\frac{\Gamma_{43}+\Gamma_{31}+\Gamma_{32}}{2}.$$

In the above density matrix equations [Eqns (2)], the diagonal elements ρ_{ii} ($i = 1-4$) denote the atomic population distribution terms, while the off-diagonal elements ρ_{ji} ($i \neq j$) denote the atomic coherence terms. The above density matrix equations are solved both numerically and analytically under the steady-state condition. The range of different numerical values of Ω_{pr}, Ω_p and Ω_c are considered from the knowledge of the values used in Refs [23, 24] for the inverted Y-type systems. The radiative and nonradiative decay rates are taken as $\Gamma_{31} = \Gamma_{32} = 2\pi \times 5.75$ MHz, $\Gamma_{43} = 2\pi \times 0.50$ MHz and $\Gamma_{21} = \Gamma_{12} = 2\pi \times 10.0$ kHz, respectively [31, 32].

To find the analytical solution, the density matrix equations [Eqns (2)] are solved under steady-state condition by using the well known weak probe field approximation, that is, by considering the terms up to the first order of Ω_{pr}. In the case of weak probe field approximation, we have assumed that the atoms primarily remain in the ground state $|1\rangle$ which implies $\rho_{11} \approx 1$ and $\rho_{22}, \rho_{33}, \rho_{44} \approx 0$ [19, 23]. Finally, we have obtained the expression of the coherence term ρ_{31} corresponding to the probe transition $|1\rangle \rightarrow |3\rangle$:

$$\rho_{31}=-\frac{i\Omega_{pr}}{2} \times\left\{(i\Delta_{pr}-\gamma_{31})+\frac{\Omega_p^2}{4[i(\Delta_{pr}-\Delta_p)-\gamma_{21}]}+\frac{\Omega_c^2}{4[i(\Delta_{pr}+\Delta_c)-\gamma_{41}]}\right\}^{-1}. \tag{3}$$

In the above analytical solution, we have neglected the contributions of the coherence terms ρ_{24}, ρ_{42} and related decay terms following the theoretical calculations carried out by the authors in Refs [19, 23]. Besides, few other coherence terms are neglected under weak probe field approximation. On the other hand, it is to be mentioned that all the contributions coming from the different coherence terms to the absorption and dispersion spectra have been considered in the numerical solutions. Now, if we examine Eqn (3), we can find that when the pump is turned off ($\Omega_p = 0$) and the control is turned on ($\Omega_c \neq 0$), Eqn (3) reduces to the solution of a three-level Ξ-type system. Again, when the control is turned off and the pump is turned on, that is, $\Omega_c = 0$ and $\Omega_p \neq 0$, then Eqn (3) reduces to the solution of a three-level Λ-type system. Therefore, we may expect that the characteristics of both Λ- and Ξ-type sub-systems will reflect the characteristics of the inverted Y-type system.

Now, the dispersion (absorption) of an atomic medium which is governed by the real (imaginary) part of complex susceptibility χ of a medium can be written in the form [15, 30],

$$\chi=\chi'+i\chi''=\frac{N|\mu_{13}|^2\rho_{31}}{\hbar\epsilon_0\Omega_{pr}}, \tag{4}$$

where χ' and χ'' represent the real ($\mathrm{Re}\chi$) and imaginary ($\mathrm{Im}\chi$) parts of the susceptibility χ, respectively; N is the atomic number density ($\sim 10^{16}$ atoms per m^3 for Rb atoms at 298 K); ϵ_0 is the permittivity of free space ($\sim 8.854 \times 10^{-12}$ F m^{-1}); μ_{13} is the dipole matrix element that couples levels $|1\rangle$ and $|3\rangle$ associated with the probe laser ($\mu_{13} \sim 2.537 \times 10^{-29}$ C m); and $\hbar$ is the reduced Planck's constant ($\sim 1.054 \times 10^{-34}$ J s) [31]. The group index n_g of the medium is related to the dispersive properties of the medium, that is, related to $\mathrm{Re}\chi$ by the relation [15]

$$n_g=1+\frac{1}{2}\mathrm{Re}\chi+\frac{\omega_{pr}}{2}\frac{\partial\,\mathrm{Re}\chi}{\partial\omega_{pr}}. \tag{5}$$

Here ω_{pr} is the probe laser frequency ($\sim 2\pi \times 3.77 \times 10^8$ MHz) [31].

The group velocity v_g of the probe light propagating through the medium is given by the expression [15, 30]

$$v_g=\frac{c}{n_g}, \tag{6}$$

where c is the speed of light in free space ($\sim 3.0 \times 10^8$ m s^{-1}). From the above Eqn (6), it is quite natural to see that the manipulation of the group velocity v_g of the light propagating in an atomic medium, that is, the subluminal and superluminal propagation of light is based upon the values of the group index n_g. By inspecting Eqns (5) and (6), we can see that the subluminal (slow) and superluminal (fast) propagation of light may occur when $n_g > 1$ and $n_g < 1$, respectively [33]. This ultimately governs the manipulation of the group velocity v_g of the light propagating in an atomic medium. The n_g values can be calculated from the knowledge of the dispersive slopes $\partial \mathrm{Re}\chi/\partial\omega_{pr}$ of the dispersion curve $\mathrm{Re}\chi$ [see Eqn (5)].

3. Results and discussion

In this section, we first observe the EIT and its dispersion signals in the proposed inverted Y-type system for which the numerically obtained probe absorption $\mathrm{Im}\chi$ and dispersion $\mathrm{Re}\chi$ profiles are plotted against the probe frequency detuning Δ_{pr} with on-resonance conditions of the pump and control lasers ($\Delta_p = \Delta_c = 0$). The dependences of the group index n_g on Δ_{pr} are studied both numerically and analytically from the knowledge of the slope of the dispersion curves. Next, we present both the numerical and analytical results of the probe absorption, dispersion and group index n_g spectra as a function of Δ_{pr} under the on/off-resonance conditions of the pump and control lasers (Δ_c, $\Delta_p \neq 0$; either Δ_c or $\Delta_p \neq 0$). The effects of the individual strengths of the pump (Ω_p), control (Ω_c) and probe (Ω_{pr}) laser fields on the $n_g(\Delta_{pr})$ profiles (with $\Delta_p = \Delta_c = 0$) have also been investigated both numerically and analytically. Moreover, the effects of the ground state decoherences ($\Gamma_{21} = \Gamma_{12}$) on the dependence of n_g on Δ_{pr} have been investigated both numerically and analytically. Finally, the dependences of the group index n_g and probe absorption $\mathrm{Im}\chi$ on both control (Ω_c) and pump (Ω_p) Rabi frequencies have been studied numerically by using both 3D and 2D plots. All the results presented in this section are discussed in detail.

3.1. Probe absorption and dispersion spectra at $\Delta_p = \Delta_c = 0$

Figure 2 shows the probe absorption ($\mathrm{Im}\chi$) and dispersion ($\mathrm{Re}\chi$) spectra as a function of probe detuning Δ_{pr}. In each plot, the probe Rabi frequency is fixed at $\Omega_{pr}/2\pi = 0.05$ MHz and the pump and control lasers are kept at resonance, that is, $\Delta_p = \Delta_c = 0$. Figures 2a and 2b display the absorption and dispersion spectra, respectively when the pump field is turned on ($\Omega_p/2\pi = 5$ MHz) and the control field is turned off ($\Omega_c/2\pi = 0$). In this case, the system is a pure three-level Λ-type configuration. We observe a single EIT window formed in a Lorentzian shape absorption dip at the line centre ($\Delta_{pr} = 0$) (Fig. 2a). Figure 2b shows the steep dispersion curve corresponding to Fig. 2a and the slope is positive at around $\Delta_{pr} = 0$. Next, we turn off the pump field ($\Omega_p/2\pi = 0$) and turn on the control field ($\Omega_c/2\pi = 8$ MHz) by which the system becomes a pure three-level Ξ-type configuration. In this case, a similar type of features of the EIT window in the absorption spectrum is shown in Fig. 2c, and the related dispersion spectrum is presented in Fig. 2d. However, it is found that the EIT width is narrower in Fig. 2a than in Fig. 2c and consequently, the dispersion curve in Fig. 2b is much steeper (positive slope with a higher value) than the dispersion curve in Fig. 2d. The above-obtained results are quite consistent with the fact that the Λ-type system is ideal for the observation of EIT and its dispersion than the Ξ-type configuration [12].

Figures 2e and 2f correspond to the case when we turn on both the pump and control fields with $\Omega_p/2\pi = 5$ MHz and $\Omega_c/2\pi = 8$ MHz, respectively. In this case, the system becomes a four-level inverted Y-type system, which is an amalgamation of three-level Λ- and three-level Ξ-type sub-systems. Hence, the nonlinear optical properties of the inverted Y-type system will have some characteristics of either a Λ- or a Ξ-type system [19, 23]. Here, it is found that the amplitude and width of the resultant EIT window increase due to simultaneous action of both the pump and control fields (Fig. 2e). Besides, we have also found a very narrow and small 'spike' (EIT-spike) on top the resultant EIT window (shown in the inset of Fig. 2e). The reason behind this spike is the superposition of two independent EIT peaks at $\Delta_{pr} = 0$ obtained from the contribution of the two individual Λ- and Ξ-type sub-systems at $\Delta_p = \Delta_c = 0$. This observation agrees well with the earlier results presented in Ref [19]. It is observed that the width of the EIT-spike is narrower than the individual Λ- or Ξ-type EIT width. The respective dispersion curve of Fig. 2e is shown in Fig. 2f where we have obtained a positive dispersion slope for the large EIT signal at around $\Delta_{pr} = 0$ and an additional sharp small positive slope is also observed at $\Delta_{pr} = 0$ due to the sharp EIT-spike on top of the EIT window (shown in the inset of Fig. 2f). Next, we have increased the strengths of the pump and control fields proportionately up to $\Omega_p/2\pi = 20$ MHz and $\Omega_c/2\pi = 30$ MHz. We have found that the width of the resultant EIT signal increases (Figs 2g and 2i) and the corresponding dispersion curves become wider (Figs 2h and 2j). At the same time, the amplitudes of the EIT-spike and the related dispersive signals (shown in the inset of Figs 2e–2j) decrease with increasing pump and control field strengths, which is due to the power broadening effect of the strong pump and control fields. The above features of the dispersion profiles are used to calculate and discuss the group index of the medium under various conditions in the next sub-sections.

3.2. Group index profiles at $\Delta_p = \Delta_c = 0$

Following Eqn (5), we have calculated both numerically and analytically the group refractive index n_g of the medium using $\mathrm{Re}\chi$ and $\partial \mathrm{Re}\chi/\partial\omega_{pr}$ data. In Fig. 3, we have plotted numerically (left panels) and analytically (right panels) obtained dependences of n_g on Δ_{pr} under the resonance conditions of the pump and control fields ($\Delta_p = \Delta_c = 0$). The probe Rabi frequency is always fixed at $\Omega_{pr}/2\pi = 0.05$ MHz for each plot. Here, we have taken $\Omega_p/2\pi = 20$ MHz and $\Omega_c/2\pi = 30$ MHz (used in Fig. 2) for which the dependences of n_g on Δ_{pr} show prominent features at $\Delta_{pr} = 0$ (Figs 3c and 3f). Now, similar to Fig. 2, we first consider the case when the control field is turned off ($\Omega_c/2\pi = 0$) and the pump is turned on ($\Omega_p/2\pi = 20$ MHz). Figure 3a displays the group index profile of the system (three-level Λ-type) where a small positive hump-like feature is observed at around $\Delta_{pr} = 0$. Next, we consider the case for which the pump field is turned off ($\Omega_p/2\pi = 0$) and the control field is turned on $\Omega_c/2\pi = 30$ MHz), that is, three-level Ξ-type system (Fig. 3b). Here, the positive hump-like feature disappears at around $\Delta_{pr} = 0$, but two strong positive

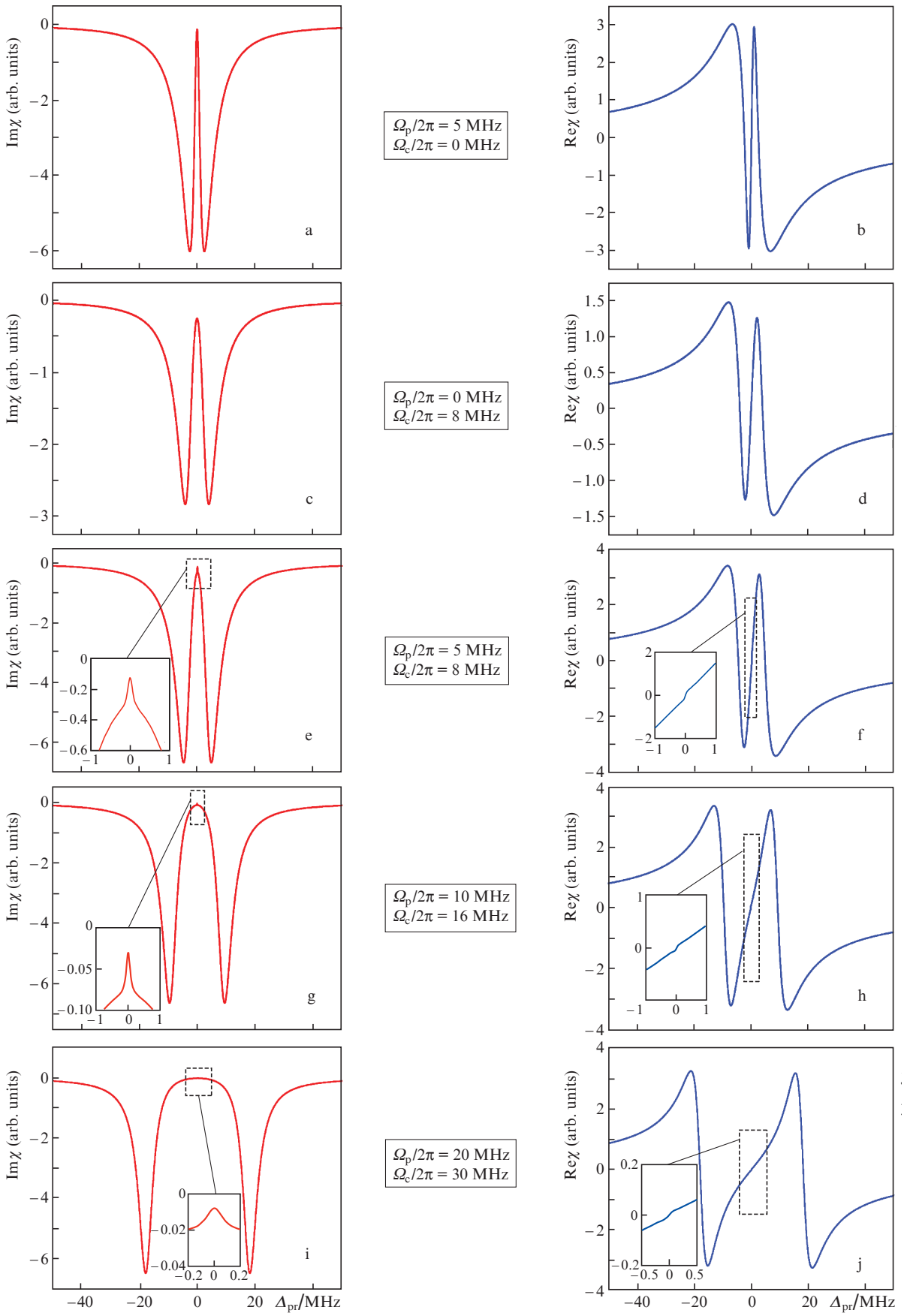

Figure 2. (Colour online) Results of numerical calculations of probe absorption (Imχ) and probe dispersion (Reχ) spectra as a function of probe detuning Δ_{pr} at different values of the pump (Ω_p) and control (Ω_c) Rabi frequencies. In all cases, the probe Rabi frequency is $\Omega_{pr}/2\pi = 0.05$ MHz and the detunings of the pump and control lasers are fixed at $\Delta_p = \Delta_c = 0$.

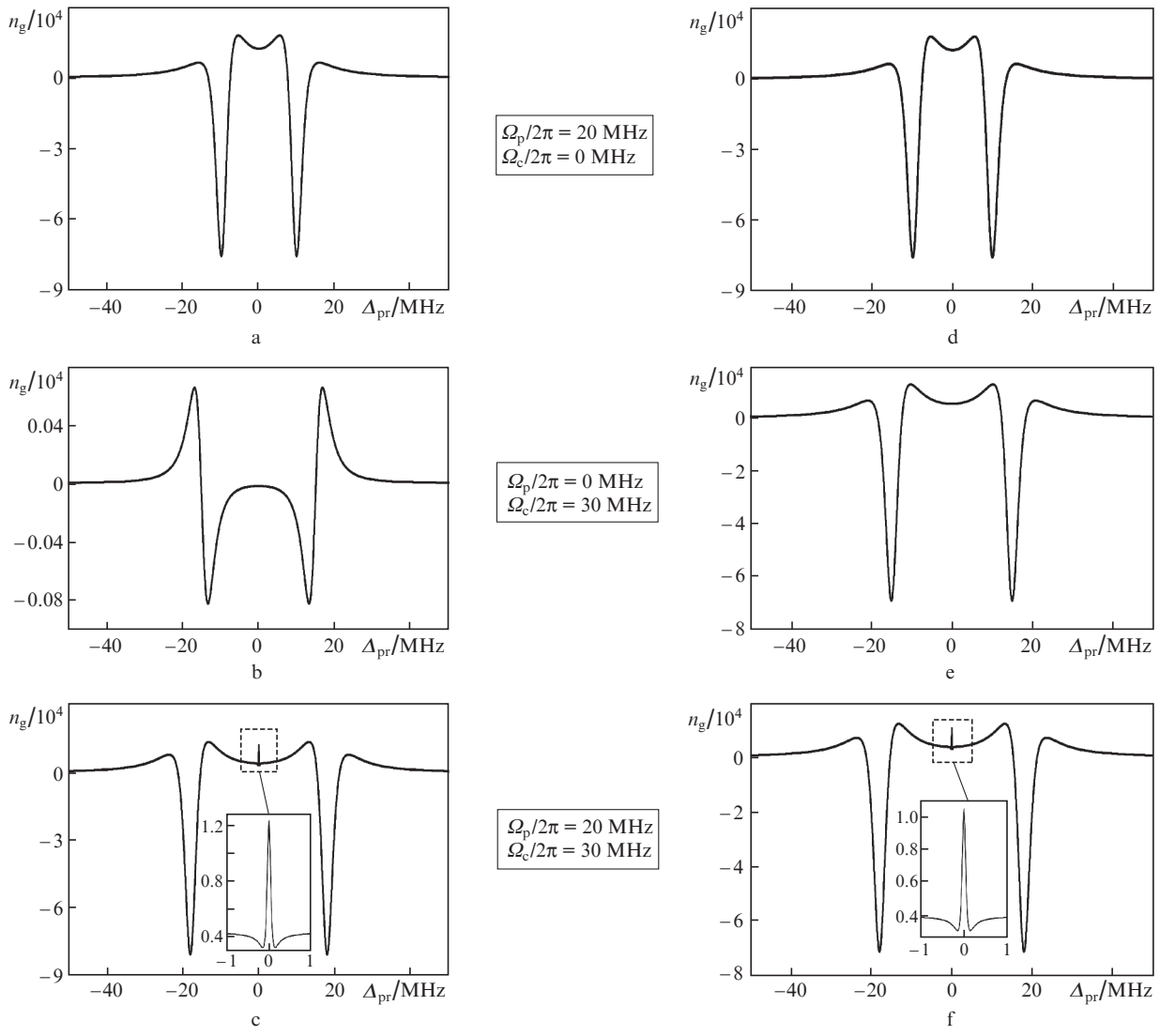

Figure 3. Results of (a, b, c) numerical and (d, e, f) analytical calculations of the group index n_g as a function of probe detuning Δ_{pr} at different pump (Ω_p) and control (Ω_c) Rabi frequencies. In all cases, the probe Rabi frequency is $\Omega_{pr}/2\pi = 0.05$ MHz and the detunings of the pump and control lasers are fixed at $\Delta_p = \Delta_c = 0$.

wings of n_g peaks are formed at both sides of $\Delta_{pr} = 0$ ($\Delta_{pr} > 0$ and $\Delta_{pr} < 0$). Now, when we switch on both the pump and control fields ($\Omega_p/2\pi = 20$ MHz and $\Omega_c/2\pi = 30$ MHz), we can see that an interesting feature is revealed by the n_g curve at $\Delta_{pr} = 0$: a very narrow positive spike of n_g is formed on top of the wide positive hump of the n_g curve at $\Delta_{pr} = 0$ (Fig. 3c). The reason behind this positive spike of the n_g value at $\Delta_{pr} = 0$ is revealed from the nature of the spike on the EIT window and the related dispersion curves obtained in Figs 2e–j. Moreover, in Figs 3a–3c, we have also found negative n_g dips for the non-zero values of probe frequency detuning, that is, at both sides of $\Delta_{pr} = 0$ ($\Delta_{pr} > 0$ and $\Delta_{pr} < 0$). The formation of these negative n_g dips is explained by the existence of negative slopes of the dispersion curves for $\Delta_{pr} > 0$ and $\Delta_{pr} < 0$ in Figs 2b, 2d, 2f, 2h and 2j. Therefore, depending on the position of probe frequency detuning Δ_{pr}, there exist both positive and negative slopes ($\partial \mathrm{Re}\chi/\partial\omega_{pr}$) of the dispersion Re$\chi$ curves in Fig. 2, which leads to both positive and negative values of n_g in Fig. 3. Now, curves in Figs 3d–3f show the respective analytically obtained dependences of n_g on Δ_{pr} for the same set of parameters used in Figs 3a–3c. We notice that the analytical curves are in good agreement with the numerically obtained curves except in Figs 3b and 3e. In Fig. 3e, the analytical curve shows a widened positive hump-like feature at around $\Delta_{pr} = 0$, while in Fig. 3b this feature is absent. This difference may arise due to some approximations made in the analytical solution of Eqn (3) in the case of a weak probe field ($\Omega_{pr}/2\pi = 0.05$ MHz), specifically, due to neglecting the coherence terms ρ_{24}, ρ_{42}, some other coherence and related decay terms in the analytical solution. Thus, the n_g curves of the inverted Y-type system having a positive hump around $\Delta_{pr} = 0$ and a spike at $\Delta_{pr} = 0$ can be used for the manipulation of group velocities v_g of the probe light in the EIT-induced medium.

3.3. Probe absorption, dispersion and group index spectra at $\Delta_p \neq \Delta_c \neq 0$

Figure 4 shows the numerical plots of absorption (Imχ), dispersion (Reχ) and group index (n_g) spectra as a function of probe detuning Δ_{pr} at $\Delta_p \neq \Delta_c \neq 0$ and either Δ_c or $\Delta_p \neq 0$, that

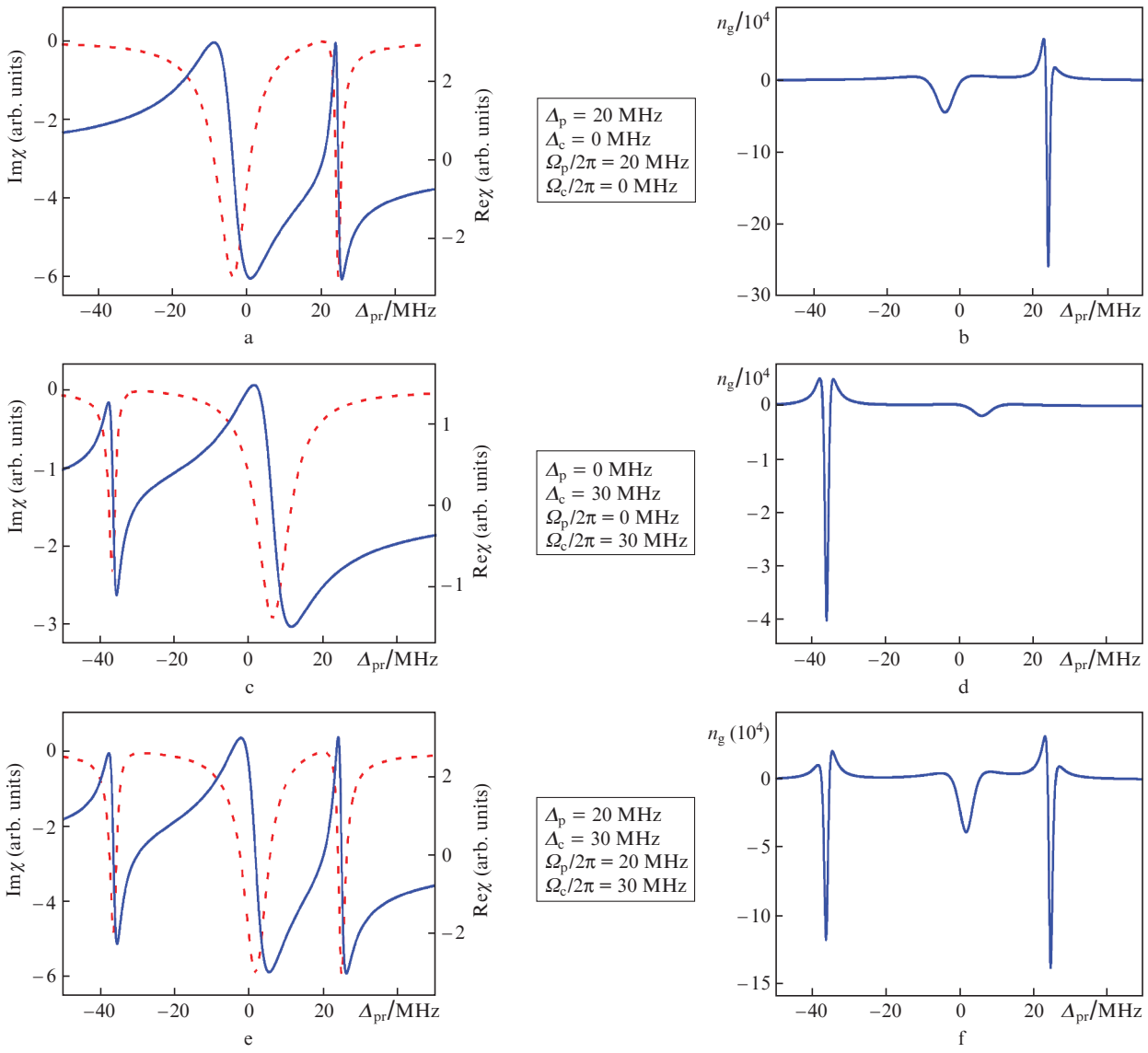

Figure 4. (Colour online) (a, c, e) Numerical calculated probe absorption (Imχ) (red dashed curve) and probe dispersion (Reχ) (blue solid curve), as well as (b, d, f) group index (n_g) profiles as a function of probe detuning Δ_{pr} at different values of the pump (Ω_p) and control (Ω_c) Rabi frequencies and their detunings Δ_p and Δ_c. In all cases, the probe Rabi frequency is fixed at $\Omega_{pr}/2\pi = 0.05$ MHz.

is, under the off-resonance conditions of the pump and/or control lasers. In each plot, the fixed value of the probe Rabi frequency is $\Omega_{pr}/2\pi = 0.05$ MHz. Figures 4a, 4c and 4e show the numerically obtained dependences of Imχ (red dashed curves) and Reχ (blue solid curves) on Δ_{pr}, while Figs 4b, 4d, and 4f demonstrate the respective dependences of n_g on Δ_{pr}. We first consider the case (Fig. 4a) for which the pump is turned on ($\Omega_p/2\pi = 20$ MHz) and kept at off-resonance ($\Delta_p = 20$ MHz), while the control light is turned off ($\Omega_c/2\pi = 0$ and $\Delta_c = 0$). In this case, the inverted Y-type system becomes a three-level Λ-type for which the EIT and the corresponding dispersion spectra are shifted towards $\Delta_{pr} = +20$ MHz. In addition, the shapes of the EIT and its dispersion signals are asymmetric due to the off-resonance condition of the pump field. The respective group index profile is also shifted towards $\Delta_{pr} = +20$ MHz (Fig. 4b). Now, when we turn off the pump ($\Omega_p/2\pi = 0$ and $\Delta_p = 0$) and turn on the off-resonance control light ($\Omega_c/2\pi = 30$ MHz and $\Delta_c = 30$ MHz), the system behaves like a three-level Ξ-type which displays the EIT and the related dispersion windows around $\Delta_{pr} = -30$ MHz (Fig. 4c). Figure 4d shows the respective n_g spectrum which is also shifted towards $\Delta_{pr} = -30$ MHz. Finally, in Figs 4e and 4f, when both the pump and control fields are turned on and kept at off-resonance ($\Omega_p/2\pi = 20$ MHz, $\Omega_c/2\pi = 30$ MHz, $\Delta_p = 20$ MHz and $\Delta_c = 30$ MHz), we have observed two separate EIT windows and the respective dispersion slopes at around $\Delta_{pr} = +20$ MHz and $\Delta_{pr} = -30$ MHz. At the same time, the associated group index features show two positive signatures at the respective positions of the EIT windows. In comparison to Fig. 2 ($\Delta_p = \Delta_c = 0$), the EIT and dispersive signals of Fig. 4 are asymmetric under off-resonance conditions. Moreover, under the off-resonance conditions of both pump and control fields ($\Delta_p \neq \Delta_c \neq 0$), we have found two EIT, two related dispersion slopes and associated two positive group index signatures on either side of the line centre of probe frequency detuning $\Delta_{pr} = 0$. Hence, under the off-reso-

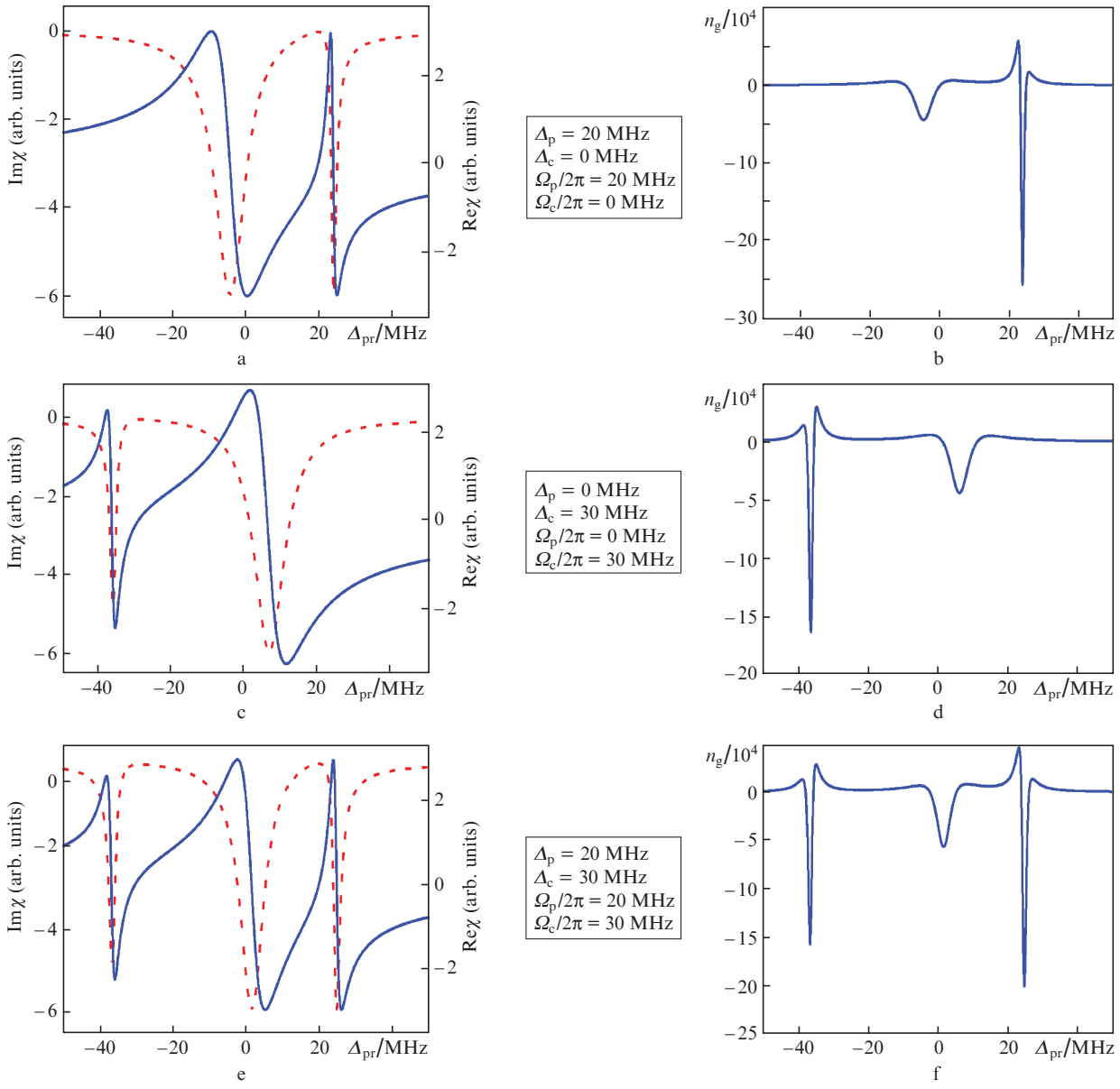

Figure 5. (Colour online) (a, c, e) Analytically calculated probe absorption (Imχ) (red dashed curve) and probe dispersion (Reχ) (blue solid curve), as well as (b, d, f) group index (n_g) profiles as a function of probe detuning Δ_{pr} at different values of the pump (Ω_p) and control (Ω_c) Rabi frequencies and their detunings Δ_p and Δ_c. In all cases, the probe Rabi frequency is fixed at $\Omega_{pr}/2\pi = 0.05$ MHz.

nance conditions of pump and control fields, the positive signatures of the group index can be obtained at two off-resonance positions of the probe detuning, while under the on-resonance conditions of pump and control fields, the tuning of the positive group index is limited around the probe detuning $\Delta_{pr} = 0$. Therefore, we can say that the shape and position of the EIT, related dispersion and the associated group index curves are much richer and can be better controlled in an inverted Y-type system under off-resonance conditions rather than under the on-resonance conditions [19]. Besides, Fig. 5 shows the analytical plots of Imχ, Reχ and n_g spectra as a function of Δ_{pr} for the same set of parameters and under the same conditions of the pump and control fields as considered in Fig. 4. Comparing all plots of Figs 4 and 5, it is found that most of the analytical curves are in good agreement with the numerical ones, except for Figs 4c, 4d and Figs 5c, 5d.

3.4. Effect of the pump, control and probe strengths on the dependence of n_g on Δ_{pr} at $\Delta_p = \Delta_c = 0$

In this subsection, we first study the effect of different strengths of pump Rabi frequencies (Ω_p) on the group index (n_g) profiles both numerically and analytically. The fixed probe and control Rabi frequencies are taken as $\Omega_{pr}/2\pi$ = 0.05 MHz and $\Omega_c/2\pi$ = 30 MHz, respectively. The detunings of the pump and control lasers are always kept at $\Delta_p = \Delta_c = 0$. Figure 6a shows the numerical plots of the dependence of the group index n_g on the probe detuning Δ_{pr} for different strengths of the pump field $\Omega_p/2\pi$ = 0, 5, 10, 15, 20 and 30 MHz. We first turn off the pump laser ($\Omega_p/2\pi = 0$) and we see that no positive hump is observed at around $\Delta_{pr} = 0$ (black colour solid *i* line), which is also consistent with the numerical result of Fig. 3b. Next, we turn on the pump and set it at

$\Omega_p/2\pi$ = 5 MHz. The group index curve displays two symmetrical positive humps (at both sides of Δ_{pr} = 0) accompanied by a very narrow spike at Δ_{pr} = 0 (red colour dashed *j* curve). This n_g spike belongs to both negative and positive regions. When the pump Rabi frequency is set at $\Omega_p/2\pi$ = 10 MHz, it is found that two symmetrical positive humps at both sides of Δ_{pr} = 0 are converted into symmetrical negative dips and a wide positive hump of the n_g is found at around

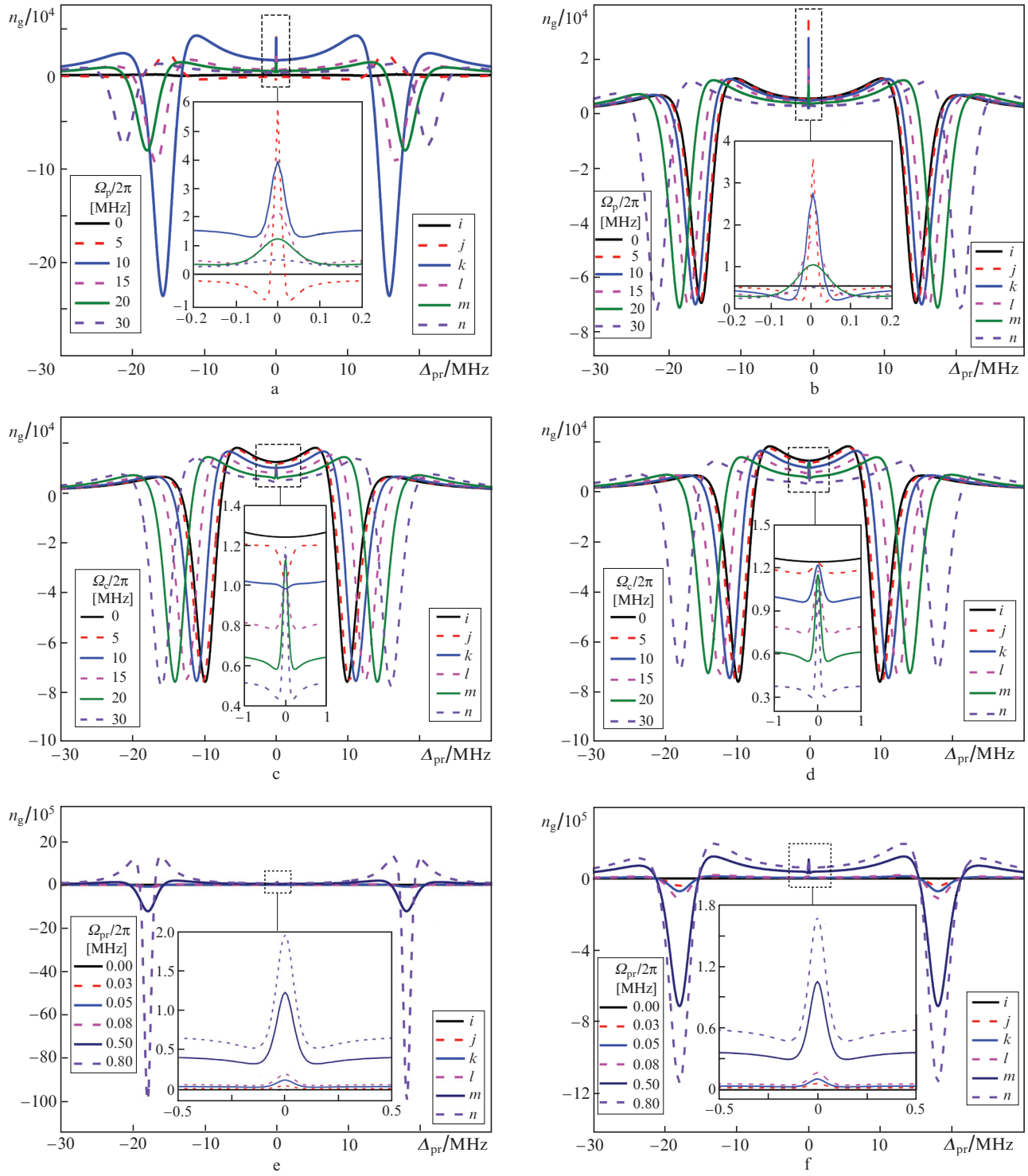

Figure 6. (Colour online) (a, c, e) Numerically and (b, d, f) analytically calculated dependences of the group index n_g on probe detuning Δ_{pr} for the different values of Ω_p, Ω_c and Ω_{pr}. In panels a and b, $\Omega_p/2\pi$ = 0, 5, 10, 15, 20 and 30 MHz (shown in the inset) at fixed $\Omega_{pr}/2\pi$ = 0.05 MHz and $\Omega_c/2\pi$ = 30 MHz; in panels c and d, $\Omega_c/2\pi$ = 0, 5, 10, 15, 20 and 30 MHz (shown in the inset) at fixed $\Omega_{pr}/2\pi$ = 0.05 MHz and $\Omega_p/2\pi$ = 20 MHz; in panels e and f, $\Omega_{pr}/2\pi$ = 0.00, 0.03, 0.05, 0.08, 0.50 and 0.80 MHz (shown in the inset) at fixed $\Omega_p/2\pi$ = 20 MHz and $\Omega_c/2\pi$ = 30 MHz. In all cases, the pump and control lasers are fixed at resonance ($\Delta_p = \Delta_c = 0$).

$\Delta_{pr} = 0$, which is similar to the pattern of n_g in Fig. 3c (blue colour solid *k* curve). At the same time, the spike becomes only positive and the amplitude of the positive spike of n_g at $\Delta_{pr} = 0$ decreases with increasing Ω_p (blue colour solid *k* curve, shown in the inset). Further, when we gradually increase the pump Rabi frequency up to 15, 20 and 30 MHz, the amplitude of the positive spike at $\Delta_{pr} = 0$ and the symmetrical negative dips at both sides of $\Delta_{pr} = 0$ also decrease gradually (magenta colour dashed *l*, green colour solid *m* and purple colour dashed *n* curves). Particularly, the negative dips of n_g curves at both sides of $\Delta_{pr} = 0$ decrease in amplitude after the value of $\Omega_p/2\pi = 10$ MHz and are shifted away from each other with an increase in $\Omega_p/2\pi$ up to 30 MHz. The analytical curves (Fig. 6b) also reveal almost similar patterns, only the noticeable difference at $\Omega_p/2\pi = 0$ is that there exists a small positive hump around $\Delta_{pr} = 0$ (black colour solid *i* curve in Fig. 6b). This is similar to the analytical curve of Fig. 3e. In the case of analytical plots, all the spikes belong to the positive region only. At $\Delta_{pr} = 0$, it is found that the amplitude of the spike decreases with increasing pump Rabi frequency for all the cases (from 5 to 30 MHz) both in numerical and analytical plots (shown in the inset of Figs 6a and 6b). Besides, we observe that there occurs symmetrical shifting of the negative dips with an increase in the values of Ω_p (cf. all plots in Figs 6a and 6b). As mentioned earlier in subsection 3.2, the analytical solutions are performed with some approximations under the weak probe regime and probably this results in minor differences among the analytical and numerical curves in Figs 6a and 6b.

In Figs 6c and 6d, we have studied the numerically and analytically obtained dependences of the group index n_g on the probe detuning Δ_{pr} for the different strengths of the control field ($\Omega_c/2\pi = 0$, 5, 10, 15, 20 and 30 MHz). The other fixed parameters are $\Omega_{pr}/2\pi = 0.05$ MHz, $\Omega_p/2\pi = 20$ MHz and $\Delta_p = \Delta_c = 0$. When the control field is turned off, that is, $\Omega_c/2\pi = 0.00$ MHz, we observe a small positive hump without any spike-like features (black colour solid *i* curve), which is analogous to Fig. 3a. As the strength of the control field is gradually increased, we have found a wide positive hump of the n_g at around $\Delta_{pr} = 0$ and two symmetrical negative dips at both sides of $\Delta_{pr} = 0$. Also, as the value of Ω_c increases, the amplitude of the widened positive hump decreases and the negative n_g dips are shifted away from each other. However, at $\Delta_{pr} = 0$, we have found a positive downward spike of the n_g curve for $\Omega_c/2\pi = 5$ MHz (red colour dashed *j* curve) and the amplitude of the downward spike decreases with increasing value of $\Omega_c/2\pi$ up to 10 MHz (blue colour solid *k* curve). But, when we further increase the value of Ω_c ($\Omega_c/2\pi = 15$, 20 and 30 MHz), the downward spike again converts into a positive upward spike where the amplitude of the spike increases with increasing Ω_c (magenta colour dashed *l*, green colour solid *m* and purple colour dashed *n* curves, shown in the inset). Thus, in the case of numerical plots, a flipping of n_g values (from a positive downward spike to an upward spike) is observed at $\Delta_{pr} = 0$. This type of flipping of the n_g 'spike' may have some possible applications in the storage and retrieval of the light pulse, pulse shaping phenomena, etc. [34–36]. Next, in Fig. 6d, we have analytically studied the same dependence of n_g on Δ_{pr} for the same set of parameters used in Fig. 6c. The analytical curves of Fig. 6d reveal almost similar features as those of the numerical ones (Fig. 6c), but the analytical curves show only positive upward spikes of n_g at $\Delta_{pr} = 0$ for all the cases and the amplitudes of the spikes increase with increasing Ω_c. The differences between the analytical and numerical spikes at $\Delta_{pr} = 0$ may be due to some approximations considered in the analytical calculation under the weak probe limit (already discussed in subsection 3.2).

Next, we have studied both numerically and analytically the dependences of the group index n_g on the probe detuning Δ_{pr} for the different strengths of the probe Rabi frequency ($\Omega_{pr}/2\pi = 0.00$, 0.03, 0.05, 0.08, 0.50, 0.80 MHz); the numerical and analytical results are shown in Figs 6e and 6f, respectively. The other fixed parameters are $\Omega_p/2\pi = 20$ MHz, $\Omega_c/2\pi = 30$ MHz and $\Delta_p = \Delta_c = 0$. In Fig. 6e, when the probe light is turned off ($\Omega_{pr}/2\pi = 0$), it is expected that there exists no hump- or spike-like a feature of the n_g spectrum (black colour solid *i* line). As the probe light is turned on and set at $\Omega_{pr}/2\pi = 0.03$ MHz, there exists a very small positive spike of n_g at $\Delta_{pr} = 0$ (red colour dashed *j* curve in Fig. 6e). Further, when we increase the values of $\Omega_{pr}/2\pi$ by 0.05 and 0.08 MHz, there occurs a gradual enhancement of the positive spike at $\Delta_{pr} = 0$ and a positive hump-like feature having a very small amplitude of the n_g curve is found at around $\Delta_{pr} = 0$ (blue colour solid *k* and magenta colour dashed *l* curves). At $\Omega_{pr}/2\pi = 0.50$ MHz, the magnitude of the positive spike is increased quite considerably and also there exists a quite visible signature of the positive hump along with a set of symmetrical negative dips on both sides of $\Delta_{pr} = 0$ (indigo colour solid *m* curve). Finally, at $\Omega_{pr}/2\pi = 0.80$ MHz, a positive spike at $\Delta_{pr} = 0$ and positive humps accompanied by negative dips of n_g on either side of $\Delta_{pr} = 0$ are enhanced significantly (purple colour dotted *n* curve). In Fig. 6f, we have analytically plotted dependences of n_g on Δ_{pr} for the same set of parameters used in the numerical plots (Fig. 6e). The analytical curves exhibit almost similar features as compared with the numerical ones, although the insets of the curves show minor differences and for the whole graph, the differences are quite pronounced. These differences may arise due to some approximations considered in the analytical calculation under a weak probe limit. All the above dependences of n_g on Δ_{pr} can be explained by using the dispersion curves presented in Fig. 2. The contributions from the positive and negative slopes of the dispersion curves at $\Delta_{pr} = 0$ and both sides of $\Delta_{pr} = 0$, respectively lead to the features exhibited in Fig. 6. Particularly, at $\Delta_{pr} = 0$, the n_g spike is narrow with respect to Δ_{pr} and thus one may say that n_g is very sensitive with the variation in Δ_{pr}. Thus we may conclude that the judicious choice of the powers of the probe, pump and control fields play a vital role in the manipulation of the n_g value, that is, related group velocity v_g of light for an inverted Y-type configuration [21, 23]. Nevertheless, due to the significant variation of n_g at $\Delta_{pr} = 0$ and either side of $\Delta_{pr} = 0$ of the inverted Y-type system, one can manipulate the group velocity v_g of the probe light through the EIT-induced medium by varying the strengths of the coupling, pump and probe fields as well as the frequency detuning of the probe laser (Δ_{pr}) [15]. This may be applied for the EIT-based optical switching effect (subluminal to superluminal or vice versa).

3.5. Effect of ground state decoherence on the group index profiles at $\Delta_p = \Delta_c = 0$

In the proposed inverted Y-type system, the pump and probe lasers form a three-level Λ-type system where the ground state decoherence rates ($\Gamma_{12} = \Gamma_{21}$) play an important role in the

EIT coherent phenomenon [27–29]. The term 'decoherence' implies the loss of coherence properties of the medium leading to broadening and reduction in the EIT and its related dispersive window. The ground state decoherence in the medium arises due to various mechanisms namely, elastic and inelastic atom-atom/wall collisions, fluctuation in temperature of the medium, etc. In our work [27], we showed that the EIT line width increases and the peak height decreases with the increase in ground state decoherence rates. The respective dispersive windows also display less steep slopes with an increase in the decoherence rates. In Fig. 7a, we numerically present the effect of different ground state decoherence rates on the group index profiles n_g as a function of probe detuning Δ_{pr}. The pump, control and probe Rabi frequencies are fixed at $\Omega_p/2\pi = 20$ MHz, $\Omega_c/2\pi = 30$ MHz and $\Omega_{pr}/2\pi = 0.05$ MHz, respectively. The pump and control lasers are kept at resonance ($\Delta_p = \Delta_c = 0$). We assume that the nonradiative decay rates between the states $|1\rangle \rightarrow |2\rangle$ and $|2\rangle \rightarrow |1\rangle$ are equal in magnitude, that is, $\Gamma_{12} = \Gamma_{21}$. The ground state decoherence rates ($\Gamma_{12} = \Gamma_{21}$) are gradually varied from $2\pi \times 0.00$ MHz to $2\pi \times 0.30$ MHz. When the ground state decoherence rates are taken as $2\pi \times 0.00$ MHz, that is, in absence of any ground state decoherence rates, we have found a wide positive hump having a very small amplitude of n_g at around $\Delta_{pr} = 0$ and two symmetrical negative n_g dips at both sides of $\Delta_{pr} = 0$ (black colour solid *i* curve). However, a narrow and high amplitude positive spike of n_g is formed at $\Delta_{pr} = 0$. When we slowly increase the ground state decoherence rates, the amplitudes of both the positive hump (at around $\Delta_{pr} = 0$) and the symmetrical negative dips (at both sides of $\Delta_{pr} = 0$) increase, but the narrow positive spike at $\Delta_{pr} = 0$ gradually decreases (cf. black colour solid *i*, red colour dashed *j* and blue colour solid *k* curves). Interestingly, at $\Gamma_{12} = \Gamma_{21} = 2\pi \times 0.04$ MHz, the spike at $\Delta_{pr} = 0$ completely vanishes (magenta colour dashed *l* curve) but the value of the n_g hump is still positive (shown in the inset). Besides, there is a slight increase in the magnitude of the negative n_g dips at both sides of $\Delta_{pr} = 0$. Further, the n_g spike reappears and is inverted downward within the positive value of n_g at $\Delta_{pr} = 0$ when $\Gamma_{12} = \Gamma_{21} = 2\pi \times 0.05$ MHz (green colour solid *m* curve). Here, we notice that when the ground state decoherence rates ($\Gamma_{12} = \Gamma_{21}$) become comparable with the probe Rabi frequency (Ω_{pr}), that is, when $\Gamma_{12} = \Gamma_{21} \sim \Omega_{pr}$, a flipping from upward to downward of the positive spike is observed. Next, when the value of $\Gamma_{12} = \Gamma_{21}$ increases beyond Ω_{pr} ($\Gamma_{12} = \Gamma_{21} = 2\pi \times 0.08$ MHz and $2\pi \times 0.10$ MHz), the overall n_g curve is inverted with respect to the previous ones (indigo colour dashed *n* and purple colour solid *o* curves). Also, n_g becomes negative at around $\Delta_{pr} = 0$ and the curve is accompanied by symmetrical positive dips on both sides of $\Delta_{pr} = 0$. Particularly, at $\Delta_{pr} = 0$, the n_g spike belongs to the negative region of n_g and just crosses the $n_g = 0$ line. Therefore, there might exist some threshold value of the ground state decoherence rates ($\Gamma_{12} = \Gamma_{21}$) at which the spike flips from a positive to a negative one and vice versa. With a further increase in ground state decoherence rates at $\Gamma_{12} = \Gamma_{21} = 2\pi \times 0.30$ MHz, the value of n_g is almost zero with respect to any values of Δ_{pr} (maroon colour dashed *p* curve). Now, in the case of analytical curves (Fig. 7b), we have not found any inversion or flipping of the n_g curves with the increase in ground state decoherence rates ($\Gamma_{12} = \Gamma_{21}$). We have only found that the amplitudes of the positive n_g spikes at $\Delta_{pr} = 0$ gradually decrease with the increase in ground state decoherence rates and finally, the amplitude of the spike vanishes at $\Gamma_{12} = \Gamma_{21} = 2\pi \times 0.30$ MHz (maroon colour dashed *p* curve). The reasons behind such differences among the numerical and analytical curves may be due to the analytical solutions performed under the weak probe limit where the contributions of all the coherent and related decay terms are not accounted for (mentioned in detail in Section 2). Therefore, we may conclude that at the resonance condition of all lasers ($\Delta_p = \Delta_c = \Delta_{pr} = 0$), the group index of the atomic medium is significantly changed with the ground

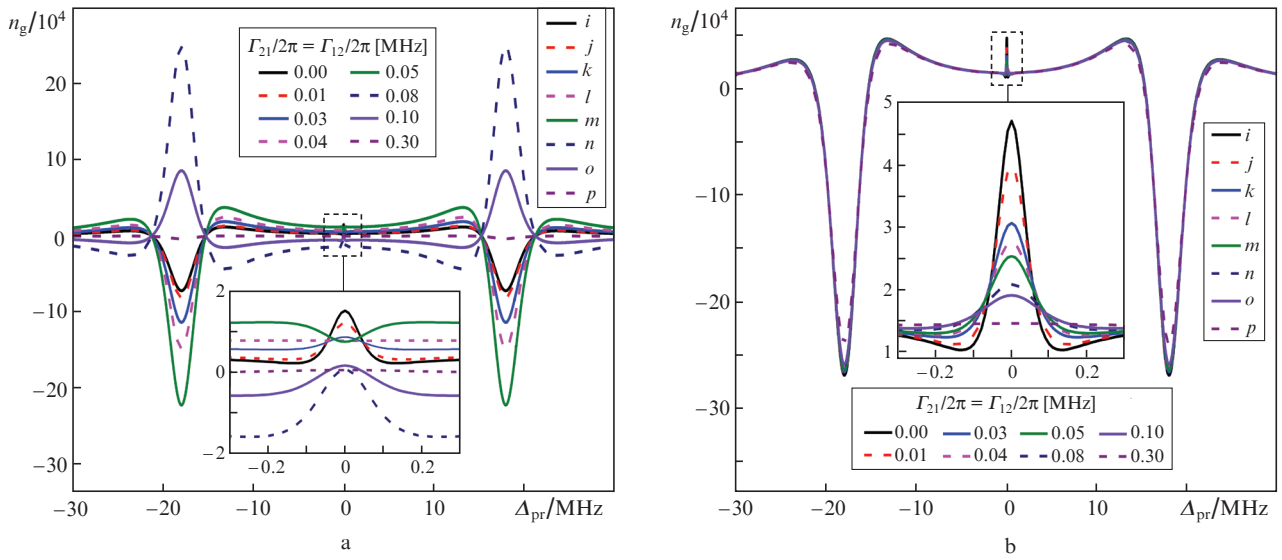

Figure 7. (Colour online) (a) Numerically and (b) analytically calculated dependences of the group index n_g on the probe detuning Δ_{pr} for the different values of nonradiative ground state decay rates $\Gamma_{12}/2\pi = \Gamma_{21}/2\pi = 0.00$, 0.01, 0.03, 0.04, 0.05, 0.08, 0.10 and 0.30 MHz. The fixed values of probe (Ω_{pr}), pump (Ω_p) and control (Ω_c) Rabi frequencies are $\Omega_{pr}/2\pi = 0.05$ MHz, $\Omega_p/2\pi = 20$ MHz and $\Omega_c/2\pi = 30$ MHz, respectively. The pump and control lasers are set at resonance ($\Delta_p = \Delta_c = 0$).

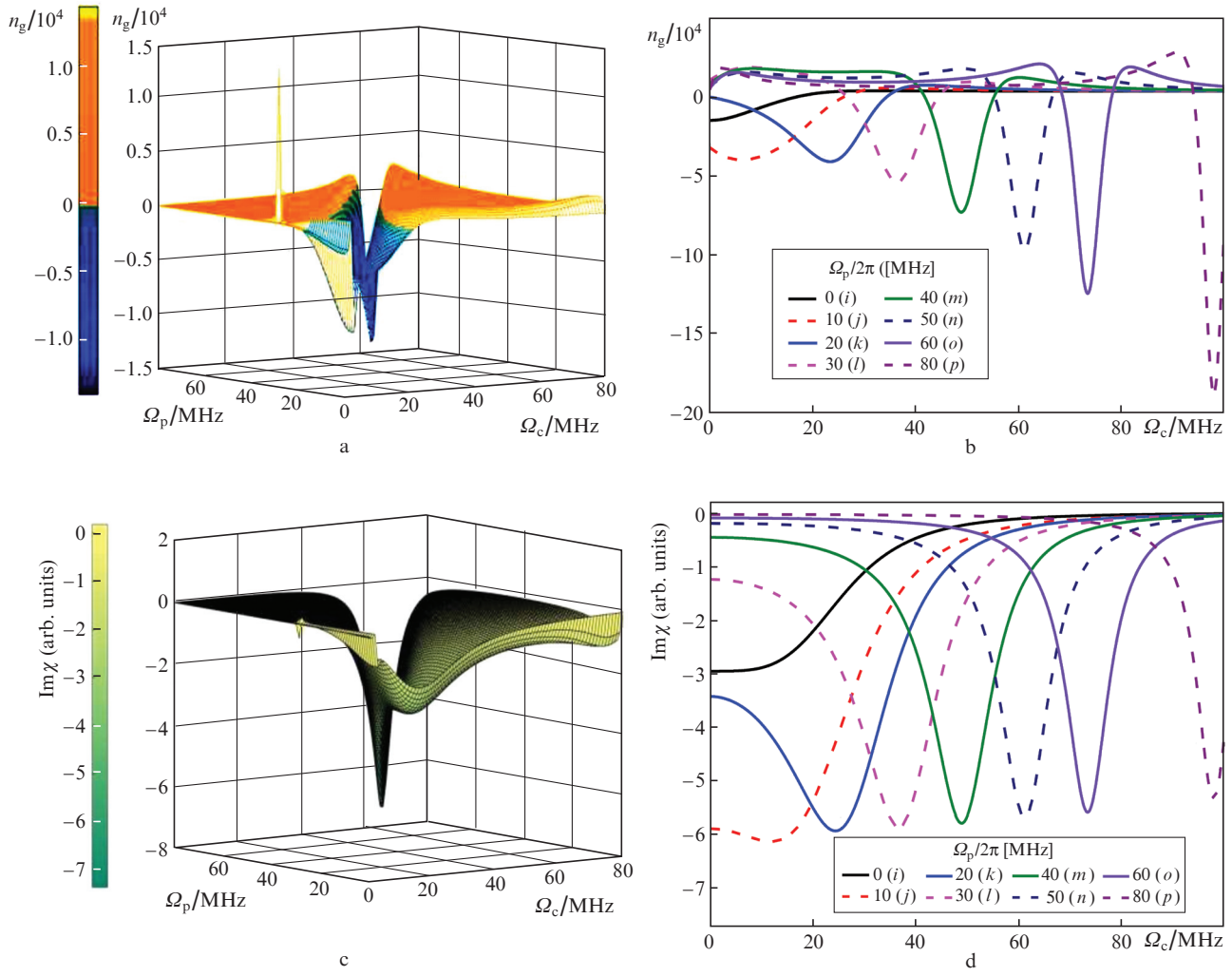

Figure 8. (Colour online) Numerically calulated 3D dependences of (a) the group index n_g and (c) probe absorption Imχ on the control Rabi frequency (Ω_c) and pump Rabi frequency (Ω_p), as well as numerically calculated 2D dependences of (b) the group index n_g and (d) probe absorption Imχ on the control Rabi frequency (Ω_c) for the different values of pump Rabi frequency (Ω_p). For all plots, the fixed parameters are $\Delta_p = 20$ MHz, $\Delta_c = 30$ MHz, $\Delta_{pr} = 0$ and the probe Rabi frequency $\Omega_{pr}/2\pi = 0.05$ MHz. The colour bar on the left-hand side of the 3D plots (a) and (c) reveals the change in magnitude of n_g and Imχ, respectively, with the variation of both Ω_p and Ω_c.

state decoherence rates which indirectly reflects the reduction or enhancement of the group velocity of the probe light.

3.6. Variation of the group index with pump and control Rabi frequencies at $\Delta_p \neq \Delta_c \neq 0$ and $\Delta_{pr} = 0$

Following the effect of pump (Ω_p) and control (Ω_c) Rabi frequencies on the group index (n_g) vs. probe detuning (Δ_{pr}) profiles (see Figs 6a–6d), here we numerically study the variation of the group index n_g with a change in both Ω_p and Ω_c at $\Delta_{pr} = 0$, $\Delta_p = 20$ MHz and $\Delta_c = 30$ MHz (Figs 8a and 8b). The fixed probe Rabi frequency is $\Omega_{pr}/2\pi = 0.05$ MHz. Figure 8a displays the 3D surface plot of group index n_g which reveals the variation of n_g with respect to the simultaneous variation of Ω_p and Ω_c. The colour bar on the left-hand side represents the change in magnitude of n_g values, where the order of the n_g value ($\sim 10^4$) is similar to Fig. 4f at $\Delta_p = 20$ MHz and $\Delta_c = 30$ MHz. The 3D curve of n_g clearly shows the existence of both positive (orange colour region) and negative (blue colour region) values of n_g and also displays a narrow spike of n_g in the positive region. The nature of the curve indicates that the value of n_g ($n_g > 1$ and $n_g < 1$) can be controlled by the variation of both pump and control field strengths, that is, the switching from subluminal to superluminal propagation of light or vice versa can be easily achieved by the simultaneous variation of Ω_c and Ω_p under off-resonance conditions ($\Delta_p = 20$ MHz, $\Delta_c = 30$ MHz). Now, to extract the value of n_g for some given values of Ω_c and Ω_p, we present the 2D figure of the group index n_g as a function of Ω_c for the different values of Ω_p (0, 10, 20, 30, 40, 50, 60 and 80 MHz) (Fig. 8b). The other parameters are the same as Fig 8a. Figure 8b also shows the existence of both positive and negative values of n_g with the simultaneous variation of Ω_p and Ω_c. Further, to understand the absorption behaviour of the medium to the probe field under the same conditions of Figs 8a and 8b, we numerically plot the probe absorption Imχ with the variation of both Ω_p and Ω_c (Figs 8c, 8d). Figure 8c shows the 3D surface plot of the probe absorption as a function of both Ω_p and Ω_c. The colour bar on the left-hand side of Fig. 8c represents the

change in magnitude of Imχ. It is found that the amplitude of Imχ decreases with increasing pump and control field strengths, that is, the medium becomes less absorptive when both Ω_p and Ω_c increase. Hence, the probe absorption, as well as probe dispersion related group index n_g of the medium can be controlled by the variation of Ω_p and Ω_c. Figure 8d shows the 2D plot of probe absorption Imχ as a function of Ω_c for the different values of Ω_p (0, 10, 20, 30, 40, 50, 60 and 80 MHz), where the amplitude of Imχ also varies with increasing Ω_c and Ω_p. Figures 8c and 8d are consistent with each other. Besides, in Figs 4 and 5, we have already seen that the tuning of the group index can be better controlled under the off-resonance conditions of the pump and control laser fields. Therefore, we may conclude that the inverted Y-type system under off-resonance conditions may be successfully used in EIT-based optical switching-based circuits [23 – 24].

4. Conclusions

In this paper, we have theoretically studied the EIT and associated dispersion spectra as well as various effects on the dispersion related group index profiles of a four-level inverted Y-type system in ^{87}Rb atomic medium. It is shown that the inverted Y-type system can be treated as a combination of three-level Λ- and three-level Ξ-type sub-systems. We have found that the absorption/dispersion spectrum and the group index profiles display characteristic features as exhibited by a typical three-level Λ- and a three-level Ξ-type system in the presence of either pump or control fields, respectively. When both the pump and control fields are turned on with resonance condition, the resultant EIT spectrum displays an enhancement along with a very sharp and narrow EIT-spike at the line centre. At the same time, the respective dispersion spectrum displays a small but steeper positive slope at the central position. The reason behind such observed spectra is explained based on the superposition of two spectra formed by the individual Λ- and Ξ-type sub-systems. Then, we have studied in detail the group index profiles of the medium, which is associated with the EIT and its dispersion spectra under various conditions. It is found that the group index profiles show both positive and negative n_g values depending on the frequency detuning of the probe laser. Particularly at the line centre, the n_g curve shows a very sharp spike and the amplitude of this spike is found to be sensitive to the variation of the strength of the applied optical fields (pump, control and probe). Besides, we have studied both numerically and analytically the absorption, dispersion and related group index (n_g) of the medium under off-resonance conditions of the pump and control lasers, revealing better control of the optical responses over a wide range of tuning of the probe laser in comparison to the on-resonance conditions. Therefore, it is possible to control the n_g values by manipulating the strengths of the applied fields and also by varying the pump, control and probe detunings. Consequently, the group velocity of the probe beam in the EIT induced medium can be manipulated from subluminal to superluminal propagation and vice versa. Further, it is found that the ground state decoherence rates also play an important role in the positive or negative values of n_g of the medium, that is, indirectly reflecting the associated group velocity of the probe beam. Finally, we have presented the phenomenon of 'EIT-based optical switching' by studying the variation of group index and probe absorption against the pump and control field strengths. Most of the numerical results are compared with the analytically obtained results. Note that the numerical results are more significant than the analytical results as the formers are obtained by taking into account all orders of the probe, pump and control Rabi frequencies as well as all the coherent and decay terms. The significant advantage of the inverted Y-type system is the bigger tunability owing to the presence of the two coupling fields (pump and control) in comparison to the three-level Λ- or Ξ-type system. The inverted Y-type system provides a richer opportunity for optical switching between subluminal and superluminal regimes. Such an optical switching phenomenon may be applicable in quantum information processing and other EIT-based switching devices.

Acknowledgements. M.M. Hossain acknowledges DHESTBT (Government of West Bengal) for sanctioning a research project [Ref. No. 249 (Sanc.)/ST/P/S&T/16G-26/2017]. We thank the reviewers for providing stimulating suggestions which greatly helped us in improving the quality of the paper.

References

1. Fleischhauer M., Imamoglu A., Marangos J.P. *Rev. Mod. Phys.*, **77**, 633 (2005).
2. Harris S.E., Field J.E., Imamoglu A. *Phys. Rev. Lett.*, **64**, 1107 (1990).
3. Harris S.E., Field J.E., Kasapi A. *Phys. Rev. A*, **46**, 29 (1992).
4. Boller K.J., Imamoglu A., Harris S.E. *Phys. Rev. Lett.*, **66**, 2593 (1991).
5. Marangos J.P. *J. Mod. Opt.*, **45**, 471 (1998).
6. Arimondo E., Orriols G. *Lett. Nuovo Cimento.*, **17**, 333 (1976).
7. Gray H.R., Whitley R.M., Stroud C.R. *Opt. Lett.*, **3**, 218 (1978).
8. Akulshin A.M., Barreiro S., Lezama A. *Phys. Rev. A*, **57**, 2996 (1998).
9. Lipsich A., Barreiro S., Akulshin A.M., Lezama A. *Phys. Rev. A*, **61**, 053803 (2000).
10. Zhou P., Swain S. *Phys. Rev. Lett.*, **77**, 3995 (1996).
11. Wang D., Zheng Y. *Phys. Rev. A*, **83**, 013810 (2011).
12. Fulton D.J., Shepherd S., Moseley R.R., Sinclair B.D., Dunn M.H. *Phys. Rev. A*, **52**, 2302 (1995).
13. Kitching J., Knappe S., Hollberg L. *Appl. Phys. Lett.*, **81**, 553 (2002).
14. Fleischhauer M., Lukin M.D. *Phys. Rev. Lett.*, **84**, 5094 (2000).
15. Hazra R., Hossain M.M. *J. Phys. B: At. Mol. Opt. Phys.*, **53**, 235401 (2020).
16. Li L., Guo H., Xiao F., Peng X., Chen X. *J. Opt. Soc. Am. B*, **22**, 1309 (2005).
17. Chen Y., Wei X.G., Ham B.S. *J. Phys. B: At. Mol. Opt. Phys.*, **42**, 065506 (2009).
18. Safari L., Iablonskyi D., Fratini F. *Eur. Phys. J. D*, **68**, 27 (2014).
19. Joshi A., Xiao M. *Phys. Lett. A*, **317**, 370 (2003).
20. Liu J.B., Liu N., Shan C.J., Huang Y.X., Liu T.K. *J. Mod. Opt.*, **56**, 1774 (2009).
21. Joshi A., Xiao M. *Phys. Rev. A*, **72**, 062319 (2005).
22. Osman K.I., Joshi A. *Opt. Commun.*, **293**, 86 (2013).
23. Yadav K., Wasan A. *Phys. Lett. A*, **381**, 3246 (2017).
24. Kou J., Wan R.G., Kuang S.Q., Jiang L., Zhang L., Kang Z.H., Wang H.H., Gao J.Y. *Opt. Commun.*, **284**, 1603 (2011).
25. Qi J. *Phys. Scr.*, **81**, 015402 (2010).
26. Yan D., Liu Y.M., Bao Q.Q., Fu C.B., Wu J.H. *Phys. Rev. A*, **86**, 023828 (2012).
27. Hazra R., Hossain M.M. *Ukr. J. Phys.*, **64**, 197 (2019).
28. Figueroa E., Vewinger F., Appel J., Lvovsky A.I. *Opt. Lett.*, **31**, 2625 (2006).

29. Erhard M., Helm H. *Phys. Rev. A*, **63**, 043813 (2001).
30. Scully M.O., Zubairy M.S. *Quantum Optics* (Cambridge, UK: Cambridge University Press, 1999).
31. Steck D.A. https://steck.us/alkalidata/rubidium87numbers.pdf (2019).
32. Tian S.C., Kang Z.H., Wang C.L., Wan R.G., Kou J., Zhang H., Jiang Y., Cui H.N., Gao J.Y. *Opt. Commun.*, **285**, 294 (2012).
33. Wang L.J., Kuzmich A., Dogariu A. *Nature*, **406**, 277 (2000).
34. Dogariu A., Kuzmich A., Wang L.J. *Phys. Rev. A*, **63**, 053806 (2001).
35. Lezama A., Akulshin A.M., Sidorov A.I., Hannaford P. *Phys. Rev. A*, **73**, 033806 (2006).
36. Tang W., Luo B., Liu Y., Guo H. *Phys. Lett. A*, **374**, 2183 (2010).